Utilizing Controlled Source Audio-Frequency Magnetotelluric (CSAMT) Method for Subsurface Structural Characterization of Wadi Rum, Southwest Jordan

Abdullah Basaloom *, Hassan Alzahrani , Mahmoud M Elwaheidi

Posted Date: 10 December 2024

doi: 10.20944/preprints202412.0763.v1

Keywords: urban sustainability; CSAMT; resistivity; subsurface structures; Gulf of Aqaba; Red Sea

 doi:10.20944/preprints202412.0763.v1

Article

Utilizing Controlled Source Audio-Frequency Magnetotelluric (CSAMT) Method for Subsurface Structural Characterization of Wadi Rum, Southwest Jordan

Abdullah Basaloom [1,*], Hassan Alzahrani [2] and Mahmoud M. El-Waheidi [2]

[1] Department of Earth Sciences and Engineering, Missouri University of Science and Technology, Rolla 65401, United States
[2] Department of Geology and Geophysics, College of Science, King Saud University, Riyadh 11451, Saudi Arabia
* Correspondence: asbvyv@mst.edu

Abstract: The UNISCO World Heritage Center announced in 2011 that the Wadi Rum Protected Area (WRPA) is a global landmark for natural and cultural attraction, which represents an emerging industrial suburban and a critical socio-economic significance to the country of Jordan. The study area in Wadi Rum is located northeast of the Gulf of Aqaba between the African and Arabian plates. The region is historically characterized by significant tectonic activity and seismic events. This study focuses on characterizing the subsurface structural features of Wadi Rum through the application of the geophysical method Controlled Source Audio-frequency Magnetotellurics (CSAMT). CSAMT data were collected from 16 sounding stations, processed, and qualitatively interpreted. The qualitative interpretation involved two main approaches: constructing sounding curves for each station and generating apparent resistivity maps at fixed depths (frequencies). The results revealed the presence of at least four distinct subsurface layers. The surface layer exhibited relatively low resistivity values (<200 Ω·m), corresponding to alluvial and wadi sediments, as well as mud flats. Two intermediate layers were identified: the first showed very low resistivity values (80–100 Ω·m), likely due to medium-grained bedded sandstone, while the second displayed intermediate resistivity values (100–800 Ω·m), representing coarse basal conglomerates and coarse sandstone formations. The deepest layer demonstrated very high resistivity values (>1000 Ω·m), which are likely attributed to basement rocks. Analysis of resistivity maps, combined with prior geological information, indicates that the subsurface in the study area features a graben-like structure, characterized by two detected faults trending in the northeast (NE) and southwest (SW) directions. The findings of this study, by providing critical insights into the subsurface structure, make a considerable contribution to the technical and scientific outlook that is necessary for the careful assessment of potential hazards and the strategic planning of future urban development within the protected area.

Keywords: urban sustainability; CSAMT; resistivity; subsurface structures; Gulf of Aqaba; Red Sea

1. Introduction

The southwest region of Jordan represents a vital social-economic importance to the country of Jordan showcasing the Wadi Rum Protected Area (WRPA) and Al-Aqaba Port connected with a railroad tracks system finally destinated to the Gulf of Aqaba (Figure 1). According to the UNISCO World Heritage Center (report finalized on June 2011 [1]), the Wadi Rum Protected Area (WRPA) is a major landmark for natural and cultural attraction for tourism which represents the most significant activity in the area. UNISCO stated that WRPA presents a diverse desert landscape characterized by narrow gorges, natural arches, significant landslides, and caverns. Evidence of human occupation

 doi:10.20944/preprints202412.0763.v1

and interaction with the environment over the past 12,000 years is manifested through petroglyphs, inscriptions, and archaeological remnants found at the site. A compilation of approximately 25,000 rock carvings alongside 20,000 inscriptions provides insight into the progression of human thought and the nascent stages of alphabet development. Furthermore, the site reflects the evolution of pastoralism, agriculture, and urbanization within the region. However, there are some concerns arisen over sustainable urban management in the longer term, including the increased random infrastructure which calls for the necessity of characterizing the subsurface regime, as well as the geohazard studies to support a future growing tourism industry in the region.

The Red Sea area is described in general as an active tectonic zone with respect to seismic functional activities [2–5]. History of active seismic zones from the north part of the Red Sea (Gulf of Aqaba) to its south base where Gulf of Aden is, shows some noticeable records of seismic activities and tectonic events [2–8]. From previous studies, it can be stated The Gulf of Aqaba, underlain by the Precambrian basement complex, has experienced an uplift. It forms an elongated, narrow depression approximately 195 km in length and 17 km in width [9], flanked by elevated mountainous regions predominantly composed of Precambrian basement rocks, resulting in very limited coastal areas. The shorelines of the Gulf are controlled by faults, appearing nearly straight with steep slopes that reflect the scarps of the surrounding faults. The study area location represents a strategic important economy located approximately 14 km NW of Wadi Rum Protected Area (WRPA) and about 40 km NE of Al-Aqaba Port along the Gulf of Aqaba (Figure 1). The region lies close to the Araba-Dead Sea Transform (DST) fault that represents an extension process of the African-Arabian composed of basement rock groups from the pre-Cambrian time. The Dead Sea Transform (DST) fault system lies on an active tectonic plate boundary that separates the African Plate from the neighboring Arabian Plate, with its formation dating back 12–18 million years. Spanning approximately 1,000 kilometers, it stretches from the northern Red Sea, through the Gulf of Aqaba, and into the territories of Jordan, Israel-Palestine, Lebanon, and Syria ([9].

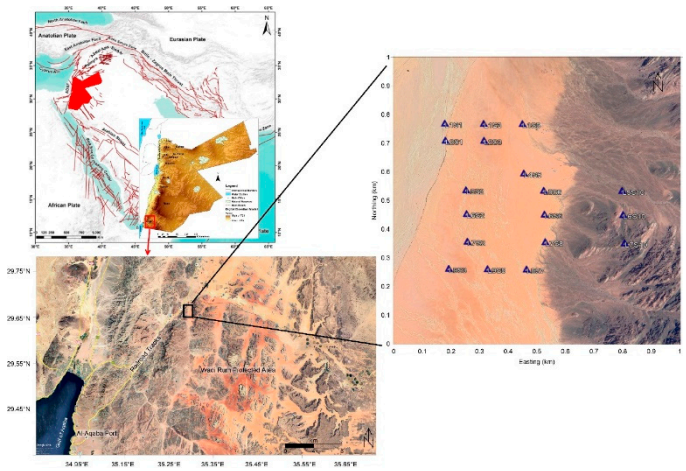

Figure 1. Location map of the study area. The overview map shows the major tectonic faults within the Arabian Peninsula obtained from [10]. The inset map describes the main topographic features of Jordan. The red square shows the map of the major important sites around the study area. The black box is the study area where blue triangles represent the MT stations laid out in the field.

Figure 2 shows seismicity and the magnetic intensity maps of the Gulf of Aqaba. Seismic data confirm that the DST fault remains active in this area. While the area generally experiences long periods of tectonic inactivity, it has occasionally recorded rare but significant earthquakes. Seismic activity within the Gulf of Aqaba and its surrounding regions (Figure 2) is most pronounced in the central sub-basin, diminishing toward the northern and southern extents [11]. While the Gulf is primarily characterized by strike-slip motion along the transform plate boundary, dip-slip extensional movements are evident along its faulted margins, accompanied by footwall uplift [12]. Analysis of elevated Pleistocene coral terraces indicates a maximum tectonic uplift of approximately

 doi:10.20944/preprints202412.0763.v1

19 meters. Subsequently, the Red Sea region underwent a complex structural evolution driven by extensional tectonics during the Oligocene-Miocene [13]. This tectonic activity was accompanied by a persistent post-Pliocene anticlockwise rotation of the Arabian Plate in relation to the African Plate, directed toward the Dead Sea Transform fault. Sedimentological analysis highlights the influence of regional structural controls on sedimentary sequences within the local basins. Quaternary faulting, widespread across the area, and associated tectonic processes have resulted in the uplift of coral reefs to approximately 6–8 meters above sea level (a.s.l.) [9]. Several studies [14–17] pointed out that in northwestern Arabia and southern Sinai, the sinistral (left-lateral) slip occurred after the emplacement of Early Neogene (20–22 Ma) dolerite dikes and NW-SE-oriented basalt flows. The cumulative displacement along the faults of the Dead Sea Transform (DST) postdates both the opening of the Red Sea and the intrusion of Early Neogene igneous dikes. Along the margins of the Gulf of Aqaba, pull-apart grabens developed between the overlapping ends of left-lateral faults [9,17,18]. Beyond the graben structures, Phanerozoic sedimentary units have been displaced downward against the basement rocks of the Precambrian period, forming several graben structures in the region. This suggests that comparable Phanerozoic sedimentary units, spanning from the Paleozoic era to the early Cenozoic, once perturbed the basement rocks of the Gulf basins. The floor systems of these graben structures are intersected by active normal faults oriented Northwest-Southeast [19]. The Dead Sea Transform (DST) functions as an active fault zone due to the ongoing divergence of the Arabian Plate from the African Plate, in conjunction with the opening of the Red Sea basin [20,21]. This tectonic activity, along with the associated seismicity in the Gulf of Aqaba, reflects the dynamic nature of the DST and its related fault systems.

Magnetic data are extensively utilized in geological investigations due to their ability to provide valuable insights into subsurface structures. Previous studies [9,16,22–24] have demonstrated that surface and subsurface faults can be effectively mapped using edge detection filters applied to magnetic data, such as the tilt derivative technique. Magnetic anomaly map in (Figure 2) shows that the study area in the Gulf of Aqaba is characterized by very low to high intensity values range from ~ (-60) nT to as high as ~ (142) nT. A The magnetic intensity map offers insights into the subsurface geology of a region, revealing features such as fault lines, volcanic activity, buried geological structures, and potential mineral deposits. It does so by highlighting zones with notably higher or lower magnetic field strength relative to the surrounding areas. The map reveals linear features, such as those represented by pink coloration, trending in multiple directions. Negative linear magnetic anomalies detected within the Gulf of Aqaba indicate ongoing displacement along both margins of the Gulf [17,25]. The residual magnetic intensity map further indicates that the eastern segment of the Gulf of Aqaba, located at the northern edge of the Arabian Shield, shares a similar geological signature with its surrounding regions. Such contrasting anomalies suggest that the area is continuously exposed to active tectonic events resulting in rifting and faulting consistent with the findings of the seismicity data. In addition, the Dead See rift zone represents a periodical continuation of some major rift structures observed from east part of Africa to the southern parts of Turkey. At local level, several major faults and lineaments; Wad Araba fault (WA), Quwaira fault (QW), and Ma'an fault (MA) dominate the area with various trends. Besides, several principal lineaments do exist in the area that has the NE-SW trend direction, with a large throw that reaches up to 250 m [26].

 doi:10.20944/preprints202412.0763.v1

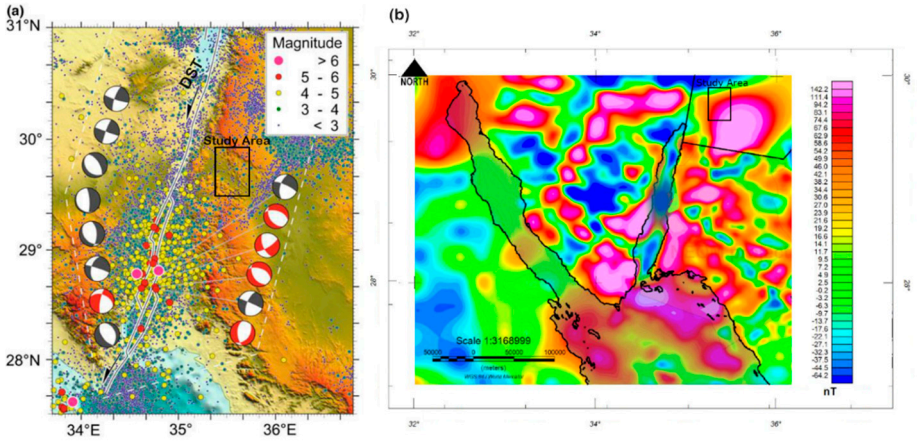

Figure 2. (a) Seismicity map showcases the earthquakes occurred in the Gulf of Aqaba. Focal mechanisms are from the Global Centroid Moment Tensor Catalog (CMT) catalogue (modified after [11]). (b) Magnetic anomaly map of Gulf of Aqaba obtained from (World Digital Magnetic Anomaly Map (WDMAM) [27] (http://wdmam.org) and modified after [9]. Black box represents the study area.

Geophysical methods are widely applied for structural and economical exploration purposes. These methods have several advantages: namely, time saving, cost saving and being noninvasive techniques [27–30]. The use of geophysical methods in structural and tectonic studies is a standard approach employed to address the absence of direct geological data [31] regarding the subsurface structures under investigation [32–37]. The controlled source audio-frequency magnetotellurics (CSAMT) is an electromagnetic frequency domain geophysical method which uses a frequency controlled artificial signal source. The CSAMT method operates by transmitting a controlled electromagnetic signal at multiple frequencies from a designated transmitter site into the subsurface [38]. The corresponding electric and magnetic fields are then measured at the receiver site within the area of interest. This technique determines the electromagnetic (EM) impedance, defined as the ratio of the horizontal electric field (E) to the orthogonal horizontal magnetic field (H). By analyzing these impedance values across various frequencies, the method provides resistivity profiles of the subsurface as a function of frequency [39]. Therefore, by controlling this source, it is possible to define the quantitative relation between the components of the electromagnetic field and determine the resistivity of the medium penetrated by these signals. The CSAMT method was first introduced by [40], who applied it in the field to detect massive sulfide anomalies. [33,41] later demonstrated the method's effectiveness in geothermal fields, confirming that the plane wave assumption holds true when the receiver-transmitter distance exceeds five skin depths. The CSAMT technique is employed to map the apparent resistivity of the subsurface, offering valuable insights into geological structures, lithology, and the presence of faults and other tectonic features [12]. Additionally, it has been shown to provide superior lateral resolution and depth of penetration compared to ground-based electromagnetic methods [42,43]. Since 1978, this low-impact geophysical survey method has been widely used in mineral, geothermal, and groundwater exploration.

The objective of this study is to investigate and map the subsurface geological and structural features of the southern part of Jordan. To overcome the challenges posed by the region's complex geological conditions and significant electromagnetic interference, we employ the CSAMT method as the primary technique for examining deep subsurface structures. This method facilitates the identification of key fault zones and geological features, offering essential insights into the area's tectonic framework. The results of this research offer significant technical and scientific contribution to the urban sustainability of the region by understanding the subsurface structural dynamics and tectonic processes.

2. Geological Setting

The geological evolution of the study area has been significantly influenced by multiple episodes of uplift and subsidence of the shield during exogenic processes. These movements have led to marine transgressions and regressions, resulting in the deposition of substantial sedimentary sequences [20,31]. The stratigraphic succession in the Wadi Rum area is generally presented in two

 doi:10.20944/preprints202412.0763.v1

distinct parts (Figure 3). The uppermost unit consists of Quaternary surface deposits, primarily composed of alluvial and groups of wadi sediments, alluvium sand, and mud flats, with a thickness of up to several meters. Beneath this, the Rum Formation is exposed, comprising continental sandstone with a maximum thickness of approximately 1 kilometer [26].

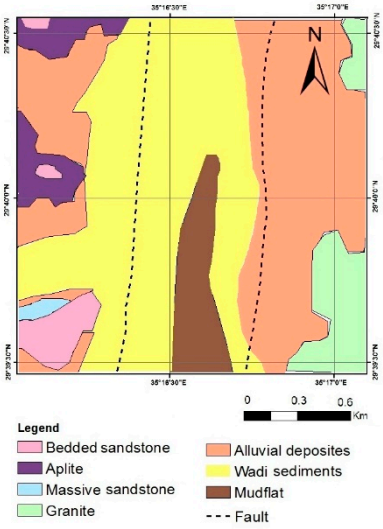

Figure 3. General geology map of the study area.

The Rum Formation is characterized by a series of sand deposits that are distinguished by their age and grain size. The initial series comprises up to 60 meters of bedded sandstone with grain sizes ranging from coarse to medium. Notably, the basal conglomerate at the base of this series can reach grain sizes of up to 0.5 meters, while medium-sized grains dominate the upper section [26]. The second series consists of coarse-grained sandstone and is notably devoid of a basal conglomerate, with a maximum thickness of 200 meters. The final series of Rum Formation is also composed of coarse-grained deposits, with a maximum thickness of approximately 300 meters.

Table 1. Stratigraphic succession in the study area [26].

Geological age	Lithology	Thickness
Quaternary deposits (youngest)	alluvial and wadi sediments, alluvium sand and mud flats	few meters (~10 m)
Rum formation	Medium-grained bedded sandstone	60 - 100 m
Continental sandstone	Coarse basal conglomerate Coarse-grained sandstone Coarse-grained massive sandstone	100 - 300 m 300 - 650 m
Precambrian Basement rocks	Granites with some granodiorite, and metamorphic rocks with some intrusive dikes	

The basement rocks of Precambrian age represent the final stage of the geological succession within the study area, predominantly consisting of granodiorite, granite, and metamorphic rocks, along with minor occurrences of acidic and basic intrusive dikes [26,31].

3. Data and Methods

The CSAMT survey profiles were spread out as east–west lines (L1, L2, L5, L6, L7, and L9) displayed in (Figure 4). This configuration was designed to examine the framework of deep fault

 doi:10.20944/preprints202412.0763.v1

structures and to conduct detailed analyses for identifying zones of lower resistivity, which in general indicate presence of fault system development.

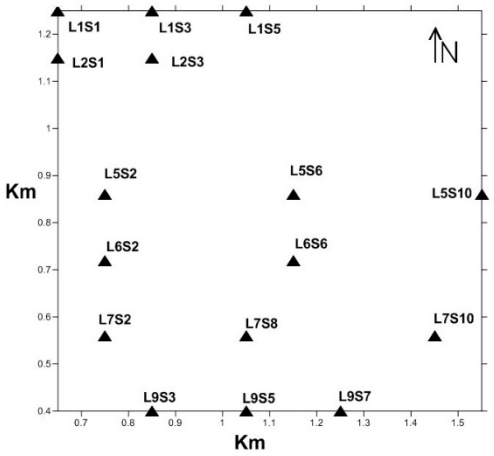

Figure 4. Field layout of the CSAMT lines with station coordinates.

During the CSAMT field configuration, we increase the distance between the transmitter and receiver to enhance the depth of exploration and minimize the effects of near-field penetration frequencies. The application of CSAMT theory relies on several key assumptions: (1) the subsurface is homogeneous or horizontally stratified; (2) the electric field within the subsurface is radial, while the magnetic field is tangential to the source; and (3) electromagnetic (EM) energy propagates as a plane wave, oriented nearly vertically downward into the subsurface. These conditions are satisfied when the energy source is positioned several wavelengths away from the measurement location.

To enhance the signal-to-noise ratio and suppress interference, several common strategies were employed: (1) utilizing high-current transmission to strengthen the effective signal, (2) increasing the spacing between receiving electrodes to amplify the electric field strength, (3) optimizing the maximum transmission–reception distance, as it is inversely proportional to the signal-to-noise ratio, and (4) using large electrode spacing for transmission [44]. Based on theoretical calculations and field experiments, the following data acquisition parameters were established: The controlled source (transmitter) consisted of two aluminum electrodes, each 1-meter square, buried in the ground approximately 1.5 kilometers apart and located several kilometers from the receiving area. The controlled frequency range spanned from 8192 Hz to 1 Hz, with a total of 14 frequency points. The plane-wave approximation was confirmed to be valid when the transmitter was positioned at distances greater than 3–5 skin depths. The field setup featured a transmitter line oriented parallel to the receiver array. The electrodes were powered by a portable generator that delivered electrical current into the ground, with saltwater applied at the electrode sites to enhance conductivity and complete the circuit. At the receiving area, a series of small porous porcelain pots were arranged in a line up to 150 meters long, interconnected by wires. These were linked to a receiver, which recorded the electromagnetic signals. After collecting the initial dataset, the pots, wires, and receiver were repositioned along the survey line to the next set of stations. This iterative process enabled data acquisition over a survey length of up to 1 kilometer. The resistivity structure of the subsurface was determined by calculating the ratio of the magnitudes of the orthogonal horizontal electric and magnetic fields (e.g., Ex and Hy). The magnitude and phase of these fields were measured at distances ranging from 500 meters to 15 kilometers from the transmitter.

The collected data was processed for interpretation and erroneous recording points were eliminated. For each valid recording point, apparent resistivity along with impedance phase data were generated versus frequency-domain. In addition, several parameters were measured and calculated for the purpose of analysis and interpretation, these include:

(1) Electric field magnitude (E) (v/m) measured from the potential differences over grounded dipoles,

 doi:10.20944/preprints202412.0763.v1

(2) Electric field phase (ϕE) (milliradians). It is defined as the phase lag between the transmitted signal and the measured electric signal. In a homogeneous Earth model, this phase lag is typically zero, with the exception occurring in the transition zone, where a noticeable change in the slope of the electric field is observed [45]. Conversely, in a non-homogeneous Earth, the phase lag deviates from zero, indicating variations in subsurface properties.

(3) Magnetic field magnitude (H) measured in A/m. This parameter is obtained from the voltage difference in a high-gain antenna.

(4) Magnetic field phase (ϕH) measured in milliradians. It is defined as the phase between the transmitted signal and the measured magnetic field signal. In a homogeneous Earth model, this phase is typically equal to - $\boldsymbol{\pi}/4$ rad in the far-field zone, where in the near-field zone it equals to zero [46]. In the case of the transition zone, it has intermediate behavior. In non-homogeneous earth, it has a complex behavior which explains the slope changes in the value of H.

(5) The apparent resistivity is calculated from the well-known Cagniard equation [32] where the ratio of the electrical field and magnetic field can be obtained:

$$\varrho a = \frac{1}{5f|H|^2}|E|^2 \quad (1)$$

The apparent resistivity (ϱa) is expressed in ohm-meters, while (f) represents the frequency in hertz, (E) denotes the electrical field magnitude in millivolts per kilometer, and (H) indicates the magnetic field magnitude in gamma. It is important to emphasize that the Cagniard equation is applicable solely in the context of plane wave configurations for the electromagnetic field, which is characterized by a sufficiently large distance between the signal transmission source and the receiving location.

(6) Phase difference (ϕ) measured in milliradians, is defined as the phase of impedance, and is normally calculated from the difference between the magnetic phase (ϕH), and the electric phase (ϕE). In homogeneous earth, the phase difference is $\boldsymbol{\pi}/4$ rad in the far-field, while it is zero in the near field. Phase difference is in proportion relationship with the slope of the resistivity log [45]; recorded values more than $\boldsymbol{\pi}/4$ indicate a higher resistive layer overlaying a less resistive one, while values lower than $\boldsymbol{\pi}/4$ indicate lower resistivity layer overlaying high resistive one.

The penetration depth of CSAMT on conductive environments is less than a skin depth [46], where skin depth (δ), measured in meters, is defined as the depth at which the amplitude of a plane wave decreases to (1/e) of its original value or 0.37%. It is given by the equation:

$$\delta = 503\sqrt{\rho/f}, \quad (2)$$

The ground resistivity (ϱ) is measured in ohm-meters, the frequency (f) is measured in radians per second [47,48]. High-frequency transmissions provide information related to shallow structures, while low-frequency transmissions are effective in probing deeper geological formations. Generally, lower frequencies correspond to a greater depth of investigation and are associated with higher ground resistivity values. However, the greater depth of investigation is usually accompanied by uncertainty levels leading to some errors. This issue is called the non-uniqueness problem which is very common in almost all geophysical methods.

Due to the existence of lateral variations in resistivity and to obtain accurate measurements, it is important to conduct both measurements of Ex/Hy and Ey/Hx. In case of Ex/Hy the greatest accuracy of measurements is obtained at the broad side and ends on to the transmitter, while in case of Ey/Hx it is centered at 45° from the transmitter [49]. Therefore, to obtain a large availability of measurements it is useful to use both Ey/Hx and Ex/Hy. Additionally, increased station spacing enhances the strength of the received signal, thereby improving the quality of the data collected.

4. Results and Discussion

CSAMT data were processed and transformed into resistivity versus depth maps, which are later interpreted into geological models. The CSAMT data collected in the study were represented in two forms for interpretation purposes; namely: sounding curves and depth maps. The obtained CSAMT sounding curves in (Figure 5) are vertically classified into four main layers according to three main factors: the expected minimum number of layers and the range of resistivity values and phase

 doi:10.20944/preprints202412.0763.v1

difference values. The sounding curves shown here for both resistivity and phase profiles are chosen based on less noise interference from the field measurements.

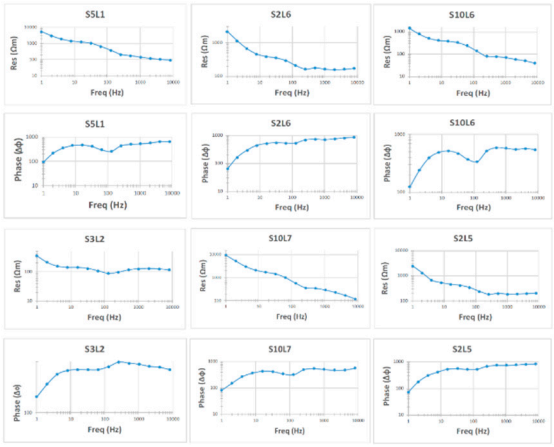

Figure 5. Typical sounding curves of resistivity and phase difference profiles for selected CSAMT stations. Resistivity is in (ohm.m) and Phase difference (Δϕ) is in milliard.

The four layers are briefly described in the following: the first layer is relatively a conductive layer with a resistivity range of 100 Ωm. This layer is shallow since it represents the youngest part (quaternary deposits) with a few meters of thickness containing alluvial and groups of wadi sediments as well as alluvium sand pockets and mud flats. The second layer is considered the most conductive layer with a very low resistivity range of about 80 Ωm because of the existence of medium-grained bedded sandstone and the absence of coarse-grained basal conglomerate. The bedded sandstone takes in place the upper part of the first series of sandstone Rum formation. The third layer is a medium-resistive layer with a range around 800 Ωm. It includes the coarse basal conglomerate at the bottom of the first sandstone series. In addition, it represents the second sandstone series (coarse sandstone) as well as the third series (coarse massive sandstone) with a total thickness of 500 m to east side of the profile. While in the west side, it appears less resistive with a resistivity less than 135 Ωm. This also represents the bottom part of the first sandstone series consisting of the coarse-grained basal conglomerate but with a range of thickness about (60 – 100) m for the whole series. The last layer is the highest resistive layer with a range above 1000 Ωm. This likely indicates deeper depth penetration into the basement rocks containing granites, granodiorite, and some metamorphic rocks with some minor intrusive dikes, which eventually by using the geophysical method (CSAMT) becomes easier to penetrate into those layers.

Based on the CSAMT data and the prior geological knowledge, it was possible to provide interpretation of fault zones and strata layering. The qualitative interpretation of the data was used to create fixed depth (fixed frequency) maps that show the aerial distribution of apparent resistivity. Several depth maps with each constructed at a fixed frequency (128 Hz, 64 Hz, 32 Hz, 8 Hz) provide, collectively, an image on the vertical variation of apparent resistivity, thus a structural interpretation could be made. Typical depth maps obtained are shown as slices in (figure 6). The selected frequencies help create a better visualization of the contrast in the resistivity profiles representing shallower and deeper structures. The measured electrical properties of the subsurface layers notably transitioned from lower resistivity zones to medium, and from medium to higher resistivity as depth increases. This variation is reflected by contour lines that extend horizontally along the survey lines.

 doi:10.20944/preprints202412.0763.v1

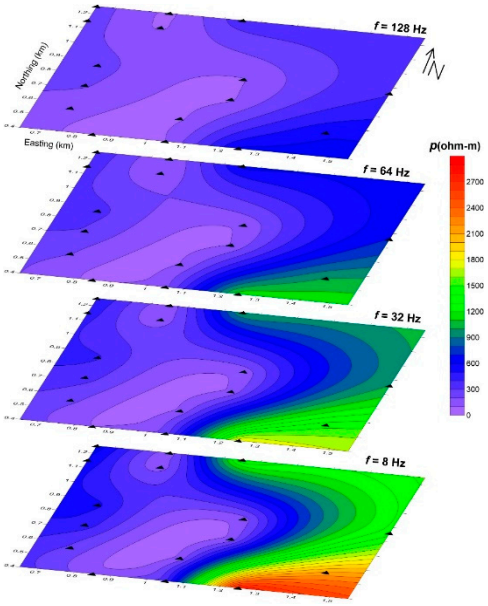

Figure 6. Typical apparent resistivity maps sliced different frequencies.

As we can notice from these maps, the blue color indicates low resistivity values, while the red one indicates higher resistivity values. It is clearly shown that at shallow depth (high frequencies), the area is mainly dominated by sediments with relatively low resistivity values. In addition to its large thickness, the penetration of these layers is small which can be inferred that this area is exposed to subsidence allowing the sediments to accumulate in large amounts there. On the contrast, maps at greater depth (low frequencies), show the presence of highly resistive formation on the eastern and western parts, while conductive sediments still can be seen at the central part of the area. To comprehensively assess the distribution of faults, a total resistivity map was created combining all frequencies from 1 Hz to 8192 Hz (Figure 7). The total resistivity map shows the resistivity contrast from the CSAMT stations, and the two suspected faults run in directions of northeast (NE) and southwest (SW).

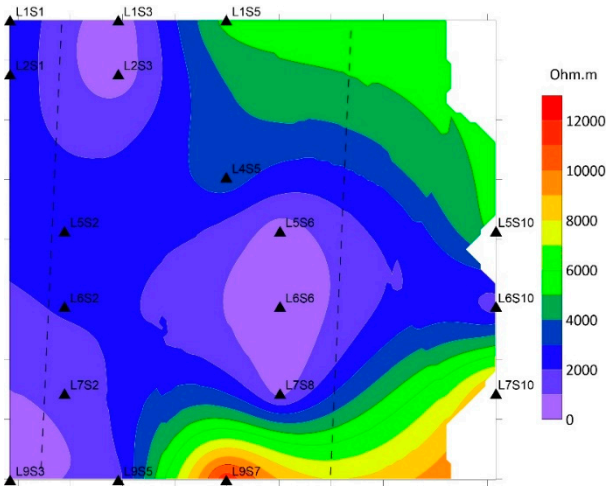

Figure 7. The total resistivity map of all frequencies. The black dotted lines referred to the two suspected faults. The black triangles are the CSAMT stations.

Based on these depth map slices and the total resistivity profile, it could be concluded that the study area has been subjected to tectonic activity that caused the uplifting of the eastern and western sides and subsidence of the central part where high thickness sediments were accumulated. This implies a two-fault system directed into NE-SW direction.

 doi:10.20944/preprints202412.0763.v1

Figure 8 highlights the observed higher resistivity values in the edged blocks of the graben, compared to the low resistivity values in its central part, can be attributed to the composition of the subsurface. The central section is predominantly composed of conductive sedimentary formations extending to significant depths. This variation in resistivity likely reflects tectonic subsidence processes that contributed to the formation of the graben structure. The CSAMT has proved to be effective in mapping the stratigraphic succession in the area and the major structural features present. The present research is an excellent case study. Furthermore, although direct geological information (borehole data etc.) is absent in the area, the qualitative interpretation of CSAMT, which is frequently used in literature, provided an efficient tool in imaging subsurface structures. However, still there is a need to optimize the derived results by conducting inversion of CSAMT and integrating other geophysical techniques.

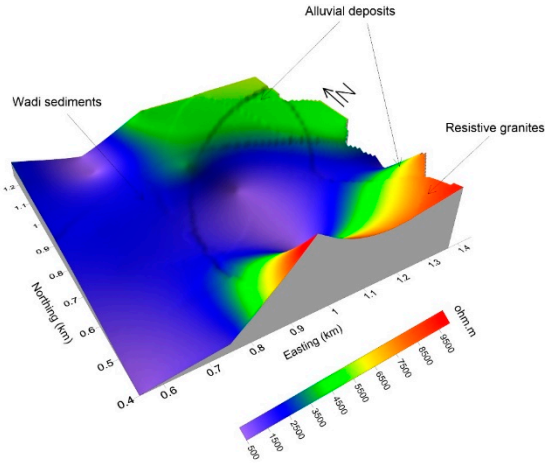

Figure 8. 3D model deduced from the apparent resistivity map in (Figure 7) of all stations explaining the associated geological and lithological information in the study area.

5. Conclusions

The analysis of the controlled source audio-frequency magnetotelluric (CSAMT) data reveals new results in the Gulf of Aqaba. The significant application of the CSAMT method lies in its ability to image subsurface conductivity with high precision. The identification of faults and structural features through CSAMT surveys provides critical information to decision-makers, aiding in the selection of areas for future hazard assessment and urban developmental planning. The results of this study demonstrate that the CSAMT technique is highly suitable and effective for investigating regions with the lack of direct geological data availability.

In conclusion, the qualitative interpretation of CSAMT data has proven to be an effective tool for mapping structural features despite the absence of direct geological information about the study area. This approach enabled the identification of the dimensional extents of a graben structure in the region with a reasonable degree of accuracy. This is postulated by two detected faults in directions of northeast (NE) and southwest (SW) run over the study area. Still, however, it is necessary to integrate multiple geophysical methods with direct geological information (boreholes) to conduct extensive geophysical investigation, hence makes an effective approach to enhance the assessment of subsurface tectonic models in urban environments.

Author Contributions: Conceptualization, A.B.; methodology, M.E.; software, A.B., and H.Z; validation, A.B., H.Z. and M.E.; formal analysis, A.B.; investigation, A.B.; resources, H.Z.; data curation, M.E.; writing—original draft preparation, A.B.; writing—review and editing, H.Z., and M.E. All authors have read and agreed to the published version of the manuscript.

Funding: This research work was supported by Reasearchers Supporting Project under grant no (RSP2024R425), King Saud University, Riyadh, Saudi Arabia.

Institutional Review Board Statement: Not applicable.

Informed Consent Statement: Not applicable.

Data Availability Statement: Data available on request from the corresponding author.

Acknowledgments: The authors would like to thank the teamwork of the Geology and Geophysics Department at King Saud University for their help in this work. Also, the authors would like to extend their gratitude to the Hadhramout Foundation for their support and assistance.

Conflicts of Interest: The authors declare no conflicts of interest. The funders had no role in the design of the study; in the collection, analyses, or interpretation of data; in the writing of the manuscript; or in the decision to publish the results.

References

1. UISCO World Heritage Center (Report on June 2011). https://whc.unesco.org/en/list/1377/#:~:text=The%2074%2C000%2Dhectare%20property%2C%20inscribed,the%20region.&text=a%20varied%20desert%20landscape,the%20region.&text=in%20the%20site%20testify,the%20region.&text=trace%20the%20evolution%20of,the%20region.
2. Izzeldin, A. Y. (1987). Seismic, gravity and magnetic surveys in the central part of the Red Sea: their interpretation and implications for the structure and evolution of the Red Sea. Tectonophysics, 143(4), 269-306. https://doi.org/10.1016/0040-1951(87)90214-9.
3. El-Waheidi, M. M., Merlanti, F., & Pavan, M. (1992). Geoelectrical Resistivity Survey of the Central Part of Azraq Basin (Jordan) for Identifying Saltwater/Freshwater Interface. Journal of Applied Geophysics, 29, 125-133. https://doi.org/10.1016/0926-9851(92)90003-4.
4. Al-Amri, A. M. S., Punsalan, B. T., & Uy, E. A. (1998). Spatial distribution of the seismicity parameters in the Red Sea regions. Journal of Asian Earth Sciences, 16(5-6), 557-563. https://doi.org/10.1016/S0743-9547(98)00046-4.
5. Al-Zahrani, H. A., Fnais, M. S., Al-Amri, A. M., & Abdel-Rahman, K. (2012). Tectonic framework of Lunayyir area, northwest Saudi Arabia through aftershock sequence analysis of 19 May 2009 earthquake and aeromagnetic data. Int. J. Phys. Sci, 7(44), 5821-5833. https://doi.org/10.5897/IJPS12.356.
6. Bender, F. (1975). Geology of the Arabian Peninsula, Jordan (No. 560-I).
7. Barberi, F., Capaldi, G., GA SPARINI, P., Marinelli, G., Santacroce, R., Scandone, R., ... & Varet, J. (1980). Recent basaltic volcanism of Jordan and its implications on the geodynamic hi-story of the Dead Sea shear zone. In Geodynamic evolution of the Afro-Arabian rift system (pp. 667-683). https://hdl.handle.net/11568/208804.
8. Basaloom, A., & Geri, M. B. (2019, June). Contribution of Rifting Activities to Spatial and Temporal Variations of Seismic B-Values Along the Gulf of Aden Area, Case Study. In ARMA US Rock Mechanics/Geomechanics Symposium (pp. ARMA-2019). ARMA.
9. Aboud, E., Alqahtani, F., Abdulfarraj, M., Abraham, E., El-Masry, N., & Osman, H. (2023). Geothermal imaging of the Saudi cross-border city of NEOM deduced from magnetic data. Sustainability, 15(5), 4549. https://doi.org/10.3390/su15054549.
10. Al-shijbi, Y., El-Hussain, I., Deif, A. et al. Probabilistic Seismic Hazard Assessment for the Arabian Peninsula. Pure Appl. Geophys. 176, 1503–1530 (2019). https://doi.org/10.1007/s00024-018-2033-4.
11. Bosworth, W., Montagna, P., Pons-Branchu, E., Rasul, N., & Taviani, M. (2017). Seismic hazards implications of uplifted Pleistocene coral terraces in the Gulf of Aqaba. Scientific Reports, 7(1), 1-13. https://doi.org/10.1038/s41598-017-00074-2.
12. Meqbel, N. M., Ritter, O., & Group, D. E. S. I. R. E. (2013). A magnetotelluric transect across the Dead Sea Basin: electrical properties of geological and hydrological units of the upper crust. Geophysical Journal International, 193(3), 1415-1431. https://doi.org/10.1093/gji/ggt051.
13. Kahal, A.Y. Geological assessment of the Neom mega-project area, northwestern Saudi Arabia: an integrated approach. Arab J Geosci 13, 345 (2020). https://doi.org/10.1007/s12517-020-05345-3.
14. Freund, R., Garfunkel, Z., Zak, I., Goldberg, M., Weissbrod, T., Derin, B., ... & Girdler, R. W. (1970). The shear along the Dead Sea rift. Philosophical Transactions for the Royal Society of London. Series A, Mathematical and Physical Sciences, 107-130.
15. Eyal, M., Bartov, Y., Shimron, A., Bentor, Y.K. (1980). Si-nai—geological map (1:500,000). Survey of Israel.

16. Aboud, E., Alotaibi, A. M., & Saud, R. (2016). Relationship between Curie isotherm surface and Moho discontinuity in the Arabian shield, Saudi Arabia. Journal of Asian Earth Sciences, 128, 42-53. https://doi.org/10.1016/j.jseaes.2016.07.025.
17. Aboulela, H. A., Aboud, E., & Bantan, R. A. (2017). Seismicity and major geologic structures of Tiran and Sanafir islands and their surroundings in the Red Sea. Environmental Earth Sciences, 76, 1-11. https://doi.org/10.1007/s12665-017-7145-0.
18. Hamimi, Z., El-Barkooky, A., Frías, J. M., Fritz, H., & Abd El-Rahman, Y. (Eds.). (2020). The geology of Egypt (p. 711). Cham: Springer. https://doi.org/10.1007/978-3-030-15265-9.
19. Ben-Avraham, Z., & Von Herzen, R. P. (1987). Heat flow and continental breakup: the Gulf of Elat (Aqaba). Journal of Geophysical Research: Solid Earth, 92(B2), 1407-1416. https://doi.org/10.1029/JB092iB02p01407.
20. Hassouneh, M. H. (2003). Interpretation of potential fields by modern data processing and 3-dimensional gravity modeling of the Dead Sea pull-apart basin/Jordan Rift Valley (JRV) (Doctoral dissertation, Universität Würzburg).
21. Khalil, S. M., & McClay, K. R. (2009). Structural control on syn-rift sedimentation, northwestern Red Sea margin, Egypt. Marine and Petroleum Geology, 26(6), 1018-1034. https://doi.org/10.1016/j.marpetgeo.2008.09.001.
22. Folkman, Y. (1980). Magnetic and gravity investigations of the Dead Sea rift and adjacent areas in northern Israel.
23. Blakely, R. J. (1996). Potential theory in gravity and magnetic applications. Cambridge university press.
24. Maus, S., Barckhausen, U., Berkenbosch, H., Bournas, N., Brozena, J., Childers, V., ... & Caratori Tontini, F. (2009). EMAG2: A 2–arc min resolution Earth Magnetic Anomaly Grid compiled from satellite, airborne, and marine magnetic measurements. Geochemistry, Geophysics, Geosystems, 10(8). https://doi.org/10.1029/2009GC002471.
25. Hildebrand, N., Shirav, M., & Freund, R. (1974). Structure of the Western Margin of the Gulf of Elat (Aqaba) in the Wadi EI Quseib-Wadi Haimur Area, Sinai. Isr. J. Earth Sci, 23, 117-130.
26. Abdelhamid, G., 1990. The Geology of Jabal Um Ishrin Area (Wadi Rum), Map sheet No. 3049 II. Bulletin 14, National Resources Authority, Amman.
27. Korhonen, J. V., Faihead, J. D., Hamoudi, M., Lesur, V., Mandea, M., Maus, S., ... & Thebault, E. (2007). Magnetic anomaly map of the world= Carte des anomalies magnétiques du monde. https://wdmam.org/.
28. Smith, J. T., & Booker, J. R. (1991). Rapid inversion of two-and three-dimensional magnetotelluric data. Journal of Geophysical Research: Solid Earth, 96(B3), 3905-3922. https://doi.org/10.1029/90JB02416.
29. Vozoff, K. (1991). The Magnetotelluric Method. In M. N. Nabighian (Ed.), Electromagnetic Methods in Applied Geophysics (Vol. 22, pp. 1943-1961). https://doi.org/10.1190/1.9781560802686.ch8.
30. Heinson, G., Direen, N. and Gill, R.M., 2006. Magnetotelluric evidence for a deep-crustal mineralizing system beneath the Olympic Dam iron oxide copper-gold deposit, southern Australia. Geology, 34, 573–576. https://doi.org/10.1130/G22222.1
31. El-Waheidi, M. M., Ghrefat, H. A., Batayneh, A., Nazzal, Y. H., & Zumlot, T. (2016). Integrated application of geoelectrical techniques for structural investigations: case study of Wadi Marsad Graben, Jordan. Arabian Journal of Geosciences, 9, 1-17. https://doi.org/10.1007/s12517-016-2466-y.
32. Cagniard, L. (1953). Basic theory of the magneto-telluric method of geophysical prospecting. Geophysics, 18(3), 605-635. https://doi.org/10.1190/1.1437915.
33. Sandberg, S. K., & Hohmann, G. W. (1982). Controlled-source audiomagnetotellurics in geothermal exploration. Geophysics, 47(1), 100-116. https://doi.org/10.1190/1.1441272.
34. Adepelumi, A.A., Yi, M.J., Kim, J.H. et al. Integration of surface geophysical methods for fracture detection in crystalline bedrocks of southwestern Nigeria. Hydrogeol J 14, 1284–1306 (2006). https://doi.org/10.1007/s10040-006-0051-2.
35. Mariita, N. O., & Keller, G. R. (2007). An integrated geophysical study of the northern Kenya rift. Journal of African Earth Sciences, 48(2-3), 80-94. https://doi.org/10.1016/j.jafrearsci.2006.05.008.
36. Wu, G., Hu, X., Huo, G., & Zhou, X. (2012). Geophysical exploration for geothermal resources: an application of MT and CSAMT in Jiangxia, Wuhan, China. Journal of Earth Science, 23(5), 757-767. https://doi.org/10.1007/s12583-012-0282-1.
37. Basaloom, A. (2020, November). 3D Seismic Interpretation in Salt Basins: Analytic Review of Case Studies. In ARMA/DGS/SEG International Geomechanics Symposium (pp. ARMA-IGS). ARMA.

 doi:10.20944/preprints202412.0763.v1

38. Jones, C. J., Robinson, M. J., & Macy, J. P. (2022). Characterization of the Sevier/Toroweap Fault Zone in Kane County, Utah, using controlled-source audio-frequency magnetotelluric (CSAMT) surveys (No. 2022-5071). US Geological Survey. https://doi.org/10.5066/P9QF9PFR.
39. Zonge, K. L. "Introduction to CSAMT." Practical Geophysics II for the Exploration Geologist. Northwest Mining Association Spokane, WA, (1992). 439-523. http://zonge.com/geophysical-methods/electrical-em/csamt (last visited, 14/11/2024).
40. Goldstein, M. A., & Strangway, D. W. (1975). Audio-frequency magnetotellurics with a grounded electric dipole source. Geophysics, 40(4), 669-683. https://doi.org/10.1190/1.1440558.
41. Bai, D., Meju, M. A., & Liao, Z. (2001). Magnetotelluric images of deep crustal structure of the Rehai geothermal field near Tengchong, southern China. Geophysical Journal International, 147(3), 677-687. https://doi.org/10.1046/j.0956-540x.2001.01568.x.
42. Routh, P. S., & Oldenburg, D. W. (1999). Inversion of controlled source audio-frequency magnetotellurics data for a horizontally layered earth. Geophysics, 64(6), 1689-1697. https://doi.org/10.1190/1.1444673.
43. Streich, R. (2016). Controlled-source electromagnetic approaches for hydrocarbon exploration and monitoring on land. Surveys in geophysics, 37, 47-80. https://doi.org/10.1007/s10712-015-9336-0.
44. Zhang, H., & Nie, F. (2024). Advancing Sustainable Geothermal Energy: A Case Study of Controlled Source Audio-Frequency Magnetotellurics Applications in Qihe, Shandong. Sustainability (2071-1050), 16(15). https://doi.org/10.3390/su16156567.
45. Staelin, D. H. (2011). Electromagnetics and applications (pp. 1-442). Cambridge, MA, USA: Massachusetts Institute of Technology.
46. Zonge, K. L., & Hughes, L. J. (1991). Controlled source audio-frequency magnetotellurics. https://doi.org/10.1190/1.9781560802686.ch9.
47. Hughes, Larry J., and Norman R. Carlson. "Structure mapping at Trap Spring Oilfield, Nevada, using controlled-source magnetotellurics." First Break 5.11 (1987).
48. Lajaunie, M., Sailhac, P., & Malet, J. P. (2018, April). Controlled-Source Audio-frequency MagnetoTelluric methods from the near-to the far-field: theory and applications. In EGU General Assembly Conference Abstracts (p. 13744).
49. David Tilley, Exploration using telluric currents – MT and CSAMT (2013). Geology for Investors, last visited 1/12/2024). https://www.geologyforinvestors.com/exploration-using-telluric-currents-mt-and-csamt/.